Nuclear Materials and Energy 25 (2020) 100829

Contents lists available at ScienceDirect

Nuclear Materials and Energy

journal homepage: www.elsevier.com/locate/nme

Exploration of $Sn_{70}Li_{30}$ alloy as possible material for flowing liquid metal plasma facing components

A. de Castro *, C. Moynihan, S. Stemmley, M. Szott, D. Andruczyk, D.N. Ruzic

University of Illinois at Urbana-Champaign, 104 S. Wright Street, Urbana, IL 61801, USA

ARTICLE INFO

Keywords:
Tin-lithium alloys
Liquid metal PFCs
Wetting characteristics
Material compatibility

ABSTRACT

As an advanced alternative to solid materials, Liquid Metals (LM) may offer more resilient and feasible Plasma Facing Components (PFCs). Particularly, regarding the unavoidable material erosion/degradation produced by particle/heat fluxes in future fusion devices where much longer duty cycles are expected. Furthermore, configurations that propose a flowing LM surface can add the advantage of a continuously fresh and clean layer facing the plasma. Although lithium is the most widely tested option, tin-lithium (SnLi) alloys have been proposed to attempt to combine the positive characteristics of both pure elements and ameliorate the specific issues of lithium. In this work, the potential use of $Sn_{70}Li_{30}$ alloy in such flowing concepts has been explored by addressing several preliminary and mandatory aspects for its utilization. Key issues such as wettability and compatibility of the alloy with relevant substrates have been studied in a multidisciplinary approach. The data obtained from deposited liquid tin-lithium droplets indicates approximate wetting temperatures of 360 °C, 390 °C and 405 °C for the fresh alloy on 316 stainless steel, molybdenum, and tungsten, respectively. However, the alloy contamination appeared to strongly affect the wetting characteristics of materials, increasing their wetting temperature by ~130 °C in the worst observed cases. Interestingly, in some instances, the instability of the liquid alloy surface was observed in the form of sudden gaseous ejection. The deposited droplets were posteriorly characterized in terms of absolute composition and depth profile by Inductively Coupled Plasma-Optical Emission Spectroscopy (ICP-OES) and Secondary Ion Mass Spectrometry (SIMS-ToF). Additionally, the nature and composition of the boundaries between the substrates and alloy microparticles was investigated by Scanning Electron Microscopy (SEM), Energy Dispersive X-Ray Spectroscopy (EDS), and 3D Laser microscopy. The overall results of this post-mortem characterization revealed that first signs of corrosion induced by both alloy elements (lithium-chromium association and iron-tin intermetallic mixing) were present on 316 stainless steel after short exposures (≤3 h) at temperatures lower than 550 °C. Conversely, molybdenum and tungsten showed good compatibility with the alloy in equivalent conditions. The global implications of these results are finally addressed, focusing on the future perspectives and the more viable scenarios for the eventual utilization of these alloys in flowing liquid metal configurations.

1. Introduction

The selection of the PFCs in contact with the burning plasma, is one of the most critical issues for the development of magnetic fusion energy. For the case of DEMO reactor designs equipped with tungsten divertor tiles (selected for ITER), the unavoidable and progressive erosion, deterioration, and final destruction of the exposed solid surfaces determine a maximum lifetime of two years [1] for such elements. After this period, they would have to be unavoidably replaced, requiring a machine shutdown and significant cost. Additionally, the sputtered high Z material will contaminate the plasma, cooling it by radiation and degrading the confinement. Finally, transient events may lead to sudden, dramatic, and irreversible damage to the tungsten solid surfaces [2].

All these constraints have motivated the search for alternatives to high Z solid materials for future fusion devices that will operate under much longer duty cycles. One of the alternatives is to use a liquid metal (LM) surface. The self-healing and self-replenishing nature of liquids may avoid the degradation problem of solids, thus improving the lifetime of such components. This may remarkably affect the electricity cost

* Corresponding author.
E-mail address: alfonsodcc11@gmail.com (A. de Castro).

https://doi.org/10.1016/j.nme.2020.100829
Received 11 September 2020; Received in revised form 27 October 2020; Accepted 28 October 2020
Available online 3 November 2020

of fusion power plants [3], and consequently their viability. Furthermore, a liquid interface may dissipate thermal loads by additional mechanisms (convection, evaporation and radiation [4]) as compared to conduction alone, potentially increasing the heat flux handling beyond the limits of solid tungsten (10 MW/m^2, [5], value that may be reduced to 5 MW/m^2 in a reactor due to neutron radiation effects).

The most studied and promising liquid metal is lithium (Li). Due to its low ionization energy and atomic number (Z = 3), as well as its alkaline and very reactive chemical nature, its use offers very beneficial effects in terms of reduced wall recycling, improved confinement, low impurity plasma content and better plasma performance [6–8]. Furthermore, recent experiments with massively lithium-coated walls have shown enhanced and flattened temperature profiles in the plasma edge [9]. At reactor scale, the associated low recycling regime, characterized by higher temperature profiles over a larger volume, would increase the D-T burning efficiency offering the possibility of constructing smaller and less expensive reactors [10].

Despite these encouraging benefits there are a few drawbacks of lithium utilization. The first one is related to its vapor pressure characteristics (high evaporation rate beyond 400 °C) that limits the operational temperature for the lithium surfaces [11]. Another important issue comes from the strong affinity of lithium for hydrogen isotopes and gaseous residual impurities, which results in progressive passivation. Although this fact enables the achievement of low recycling regimes, for long pulse, reactor scale operation, it will require the development of flowing liquid metal components with a circulating, continuously refreshed lithium surface as a PFC. Additionally, although tritium control and recuperation will be mandatory regardless of the PFC choice for the reactor, the high absorption of hydrogen isotopes will require new technologies for a more controlled and frequent, even continuous, real-time tritium recuperation [12–13] in lithium-based reactors. Finally, its chemical nature demands a thorough safety protocol during operation. Such contingency justifies the desire to minimize the total amount of liquid lithium that is present at any time inside a fusion device.

The necessity of ameliorating these drawbacks and, at the same time, maintaining lithium benefits motivated the investigation of liquid tin-lithium (SnLi) alloys as plasma facing materials. As was first inferred during the APEX project [14], the hybrid material could potentially combine the positive characteristics of both pure elements. In liquid state, lithium is expected to strongly segregate to the surface [15] within a thickness range of tens of nm as has been implicitly observed in several experiments [16–18]. At the same time, the postulated vapor pressure of the alloy is three orders of magnitude lower than lithium [19]. Experiments performed in the TJ-II Stellarator [17,20] with $Sn_{80}Li_{20}$ (subscript indicates composition in at. %) demonstrated a very good compatibility of the alloy (low Z, lithium-like behavior), showing clean plasmas with no significant high Z tin impurities. $Sn_{80}Li_{20}$ and $Sn_{70}Li_{30}$ alloys have exhibited a bulk hydrogen retention much lower than lithium, similar to that of tin (below 0.1 at. %) [17,21], element that, for such reason, may be expected to be associated to high recycling plasma edge scenarios where, otherwise, the commented low recycling lithium benefits may not be accomplished. Tin-lithium alloys, however, are much less investigated that lithium or tin as liquid metal option and there is no experience in flowing liquid metal PFC configurations with it.

Regarding basic technological requirements, any liquid metal component must have the ability to properly coat the underlying solid support structure to assure its protection from plasma exposure. This is even more imperative for flowing liquid metal components where the molten layer needs to fully wet the substrate to flow homogeneously. In experiments performed on HT-7 and EAST Tokamaks with flowing liquid lithium limiters (FLiLi [22] and LiMIT [23]), absence of total lithium coverage on the substrate was reported and resulted in non-optimal operation of the PFC [24]. In recent years, the University of Illinois at Urbana-Champaign (UIUC) has studied the wetting properties of liquid lithium on fusion relevant substrates and lithium compounds [25,26]. A minimum temperature about 300–350 °C was required to wet (contact angle below critical value of 90° between liquid droplet and substrate) stainless steel, molybdenum and tungsten. Furthermore, lithium was found to generally wet its oxide, nitride and carbonate compounds at lower temperatures. Besides that, experience with Capillary Porous Systems (CPS) shows that liquid lithium on a porous mesh (size in the range of hundred microns) generally needs more than 500 °C [27] for suitable wetting/wicking. Theoretically, [28] a porous or rough surface produces larger contact angles at the microscale that hinder adequate macroscopic wetting, thus requiring a higher temperature for liquid spreading. A similar hydrophobic effect was also observed at UIUC in experiments with liquid lithium deposited on laser texturized surfaces [29]. Nevertheless, little is known about the specific behavior of SnLi alloys and pure liquid tin. Experience with CPS has implicated challenging wetting characteristics for these materials in porous substrates compared to liquid lithium [20,30], but no systematic wetting studies have been carried out with either of these LM candidates. In flowing LM PFCs, proper wetting and homogeneous distribution for flow needs to be achieved at temperatures compatible with the material vapor pressure and substrate corrosion limitations and, in the case of lithium, with gettering and efficient hydrogen absorption if low recycling is desired. Minimization of such necessary temperature is obviously convenient from any engineering and operation perspective as well.

Another important constraint that affects the utilization of liquid metals is the material compatibility. Contact with substrates can produce net mass transfer to/or from substrates even producing, in the long term, embrittlement or fracture failures [31]. Moreover, flowing liquid metal configurations can aggravate these problems by inducing dynamic erosion and/or abrasion on the solid surfaces. Different mechanisms may cause the material deterioration [32], such as solution attack, intermetallic alloying, intergranular penetration and impurity induced corrosion. Liquid lithium moderately attacks steels [33], while being compatible with high Z refractory metals like tungsten and molybdenum [32]. For liquid tin, the corrosion of steels is notoriously more severe, while compatibility with molybdenum and tungsten generally seems acceptable [32]. Finally, in the case of tin-lithium alloys, the specific corrosion studies are very scarce and limited to some steels [34]. No specific tests on molybdenum or tungsten are reported.

In an attempt to globally study the potential utilization of tin-lithium alloys in flowing liquid metal components, the UIUC has developed an experimental campaign in order to: synthetize the material, characterize it and study its wetting and compatibility with relevant substrates. Wetting experiments have been conducted with $Sn_{70}Li_{30}$ on fusion relevant materials: 316 stainless steel (316 SS), molybdenum (Mo) and tungsten (W). Additionally, the alloy has been characterized by ICP-OES and SIMS-ToF, and the mixing/chemical interaction with the substrates, produced during the wetting test, has been studied by means of SEM, EDS, 3D Laser microscopy and SIMS-ToF. The paper is structured as follows. Section 2 introduces the experimental methods devoted to fabricating the alloy, studying its wetting characteristics, determining the alloy composition, and investigating the effects produced by the mutual interaction between the substrates and the liquid metal specimens. The results of this multidisciplinary investigation are presented in Section 3. Section 4 discusses the obtained results and the related implications for the use of the alloy in flowing PFC configurations. Section 5 summarizes the main conclusions obtained from the experimental works, also mentioning the future works planned with the material.

2. Experimental methods

2.1. Synthesis of the alloy

For the synthesis of the alloy, a specific chamber containing an inductive furnace was utilized (Fig. 1). The alloy was casted twice. Each casted portion weighed around 120 g and was prepared to present a global elemental proportion of $Sn_{70}Li_{30}$. Such composition presents a

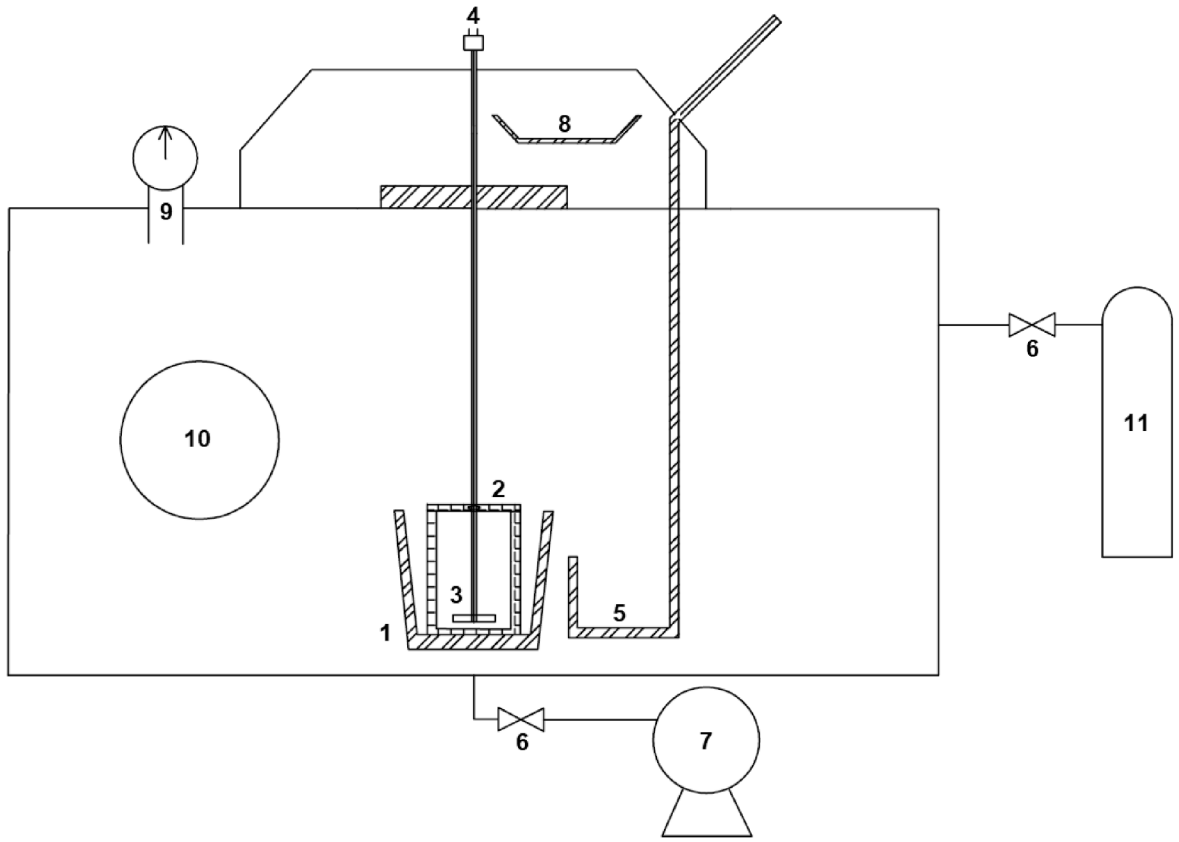

Fig. 1. Schematic view of the SnLi synthesis chamber: 1. Inductive furnace, 2. Stainless steel crucible, 3. Stirrer, 4. Thermocouple (signal output), 5. Hook manipulator, 6. Gate valves, 7. Rough pump, 8. Cooling tray, 9. Bourdon manometer, 10. Optical window, 11. Argon cylinder.

moderate melting point around 360 °C [35] and also contains an appreciable amount of lithium, necessary for maintaining the benefits of a lithium plasma material interface. The alloy casting process was carried out inside a stainless-steel crucible, placed in the commented furnace, where a stirrer is inserted from above. Before starting the procedure, a careful cleaning of the crucible and the stirrer by covering their surfaces overnight with commercial (36.5 wt% concentration) hydrochloric acid is performed. This process removes metallic impurities that, otherwise, could be incorporated into the alloy. Inside an argon pressurized glove box, the desired Sn/Li mass proportion is introduced in the crucible. Then, it is rapidly placed inside the induction heater, the chamber is closed and evacuated by means of a rough pump, and finally filled with high purity argon up to a pressure of 15 Torr. In this way, an inert environment necessary to avoid the contamination of lithium is assured. During the process, the crucible is progressively heated to melt the components, finally reaching the necessary temperature for the casting. The temperature of the mixture is measured with a K type thermocouple whose wire is introduced through the hollow bar of the stirrer until reaching the rotating head that continuously mixes both metals during the synthesis. After exceeding an approximate temperature of 500 °C, a sudden increase in the temperature of the molten mixture is observed, thus indicating the formation of the alloy (exothermic heat of formation). Then, the heating rate of the crucible is decreased to maintain a constant temperature while the mixture is continuously stirred for 10–15 min more to assure a homogeneous composition in the molten material. Finally, using a hook-shaped manipulator the crucible is flipped thus transferring the molten alloy to a metallic tray for its cooling and solidification in argon atmosphere. The fabricated alloy is stored in an argon glove box to avoid the contamination with atmospheric gases.

2.2. $Sn_{70}Li_{30}$ wetting experiments

The experiments were performed in the Material Characterization Test Stand (MCATS) apparatus, which has previously been used to measure the contact angle of liquid lithium droplets [25]. The alloy droplets (approximate size between 5 and 10 mm of diameter) were deposited on the different substrates by means of a stainless-steel liquid metal injector that has a small diameter nozzle whose tip injects the molten metal. As was observed during the experiment (see next sections), the alloy was found to interact with the stainless-steel constituents, thus complicating the differentiation of the source (substrate or injector) of iron, chromium or nickel contents present in the alloy liquid bulk after the experiments. Hence, in the future, in order to quantify this global corrosion process, the substitution of such stainless-steel injector by another one made of an element (for example tantalum), different than the studied materials, seems strongly recommendable. However for the studies presented here, the analyses were centered on specific surfaces (base of the droplet in contact with the substrate during the experiment) and regions (boundaries between alloy microdroplets and substrate) where the alloy-stainless steel interaction was delimited to the droplet-substrate case and consequently the effects of the global contamination from the injector may be considered negligible. The whole body of the injector is surrounded by a heating element that can raise the temperature beyond 600 °C (measured by K type thermocouple). The injector is coupled to a screw-type manipulator that can be operated externally to finely control the droplet size. Fig. 2a, shows the main elements of the liquid alloy injection system, while Fig. 2b shows a sketch of the droplet deposition and the subsequent measurement of the contact angle.

Beneath the injector, the different substrates are placed on a stage that contains tungsten filaments for heating up the samples. The temperature of the stage is measured at different points on the substrate

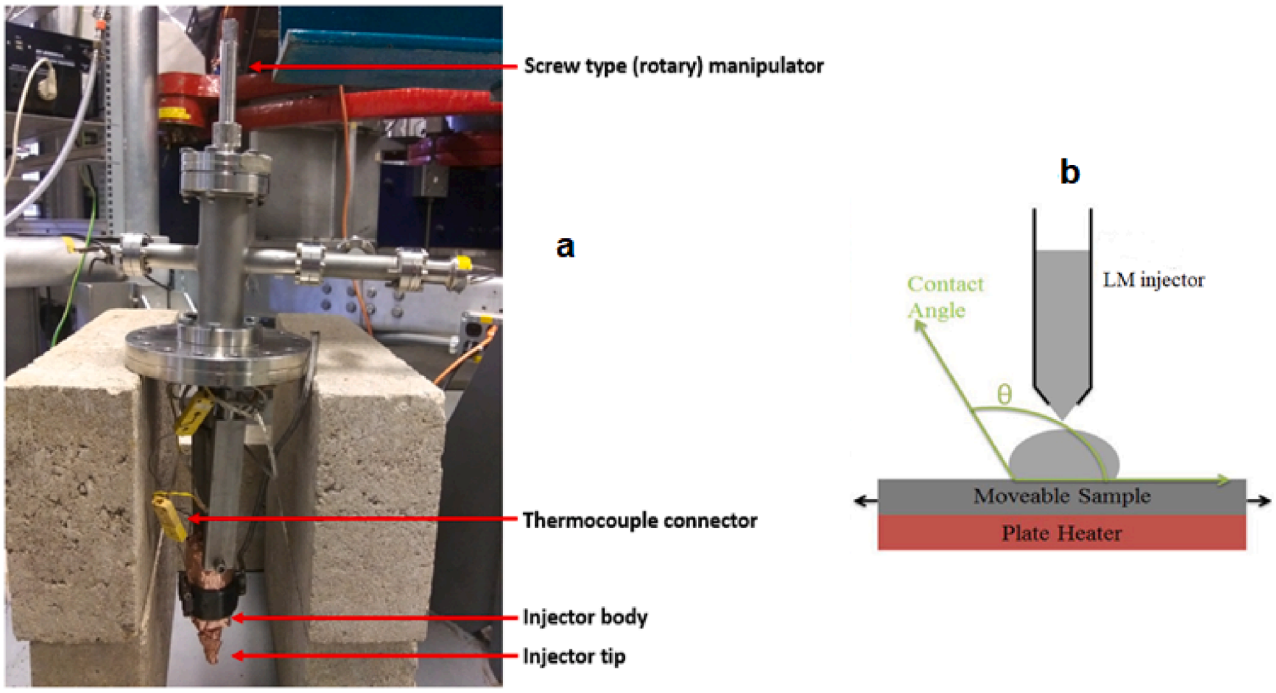

Fig. 2. a) Elements of the liquid metal injector for the wetting experiments. b) Sketch showing the droplet deposition and contact angle determination (reproduced with permission from [25]).

surface by means of K type thermocouples embedded on it. The heating stage is attached to a linear motion manipulator that allows horizontal translation, thus enabling the deposition of droplets on different points of the substrate. The whole chamber is pumped out by means of a turbomolecular pump coupled to a rough pump (base pressure in the chamber in the range of 10^{-6} Torr). Nonetheless, during the experiments the residual pressure increased due to the outgassing induced by heating, up to levels around $2 \cdot 10^{-5}$ Torr. Both the heating elements were heated up slowly (several hours) to induce progressive desorption of impurities and spatial temperature homogeneity. Measurements covered a temperature range for substrates between 350 °C and 600 °C. During each droplet deposition, the experimental strategy tried to maintain the same temperature in the injector and on the substrate to assure that droplets are at the substrate temperature. Once the droplet was on the substrate, several pictures were taken using a high definition camera. Then, the stage is horizontally moved and set at a different temperature. After that, another droplet is deposited on a different substrate portion and so forth. The analysis of the droplet picture and the determination of the contact angle was carried out with MATLAB software, using a specific image processing toolbox able to accurately trace the tangent lines to droplet surface that define the contact angle (Fig. 3).

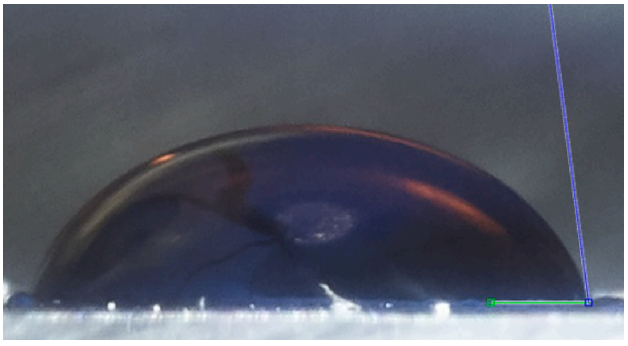

Fig. 3. $Sn_{70}Li_{30}$ alloy droplet (approximate diameter of 5 mm) showing the lines traced with MATLAB toolbox that define the contact angle.

Generally, the contact angle between a solid surface and a liquid droplet is defined by Young's equation in terms of the surface tension of the interphases:

$$\gamma_{SV} = \gamma_{LS} + \gamma_{LV}\cos(\theta) \quad (1)$$

In this expression, γ_{SV} γ_{LS} and γ_{LV} are the values for the surface tension of the solid–vacuum, liquid–solid and liquid-vacuum interphases, and θ is the contact angle. From the literature, critical wetting conditions are considered when the contact angle between the liquid droplet and the solid surface is 90°. Additionally, every surface tension value is temperature dependent, hence there exists a temperature dependence of the contact angle (and concomitant wetting pattern), which is found to decrease with temperature [25].

The experiments were performed on three different commercially purchased substrates: 316 stainless steel (316 SS), tungsten (W), and molybdenum (Mo). The average surface roughness (S_a) of the studied materials was determined by 3D profilometry. The substrates presented the following values: 40–50 nm for 316 SS (finely polished surface), 220–240 nm for Mo (commercial roughness with surface rolled just in one horizontal direction) and 700–750 nm for W (rough finished surface). To cover a wider temperature range for every material, several experimental rounds were performed during different days for every substrate.

2.3. Post-mortem characterization of alloy droplets and substrates

2.3.1. Optical emission Spectroscopy assisted by Inductively coupled plasma

This technique was utilized to determine the global composition of the prepared alloy. Tin-lithium alloy samples were dissolved in aqua regia at 220 °C for 30 min. The characteristic line emission of each element was produced by exposing the solution to an inductive argon plasma. After employing a calibration curve prepared with appropriate standards, the intensity of the collected emission was related to the absolute amount of each element present in the sample. For the quantification of tin, a line emission placed in the ultraviolet region was employed (189.93 nm) while the red Li I line (670.78 nm) was used for lithium.

2.3.2. Time of flight secondary ion mass spectrometry (SIMS-ToF)

To study their elemental depth profile and chemical composition, the surface of some alloy droplets and substrates, that were in mutual contact during the wetting experiments, were analyzed by using SIMS-ToF. The utilized equipment was a PHI TRIFT III SIMS-ToF located in the Material Research Analysis Laboratory (MRL) of the University of Illinois. This device detects a fraction of the sputtered species from the sample that are in an ionized state (secondary ions). The detector of the instrument can discriminate each secondary sputtered ion depending on its time of flight, producing a mass separation of the ejected material. For depth profiling analysis, the instrument needs to successively erode different layers of material. For this purpose, it uses a dual ion beam to run a two-phase profile cycle. During the first phase, a gold ion beam bombards the sample surface producing the gross erosion of the surface. After it, the second phase uses a different ion beam whose more accurate focusing induces a finer and more controlled ejection. The used second ion beam was O_2^+ for positive ion detection and Cs^+ beam for negative ones. During the analyses, the current of these second ion beams was around 150–250 nA, with an acceleration voltage of V = 2 kV. Both cycles of gold and O_2^+ / Cs^+ beams are alternated during the desired analysis time of the depth profile, thus progressively analyzing deeper layers of the sample.

To calibrate the depth profile measurements of the tin-lithium samples (analysis time vs sample depth), the vertical erosion rate produced by the dual beam on the alloy surface was approximated by the value corresponding to a smooth, pure tin thin film deposited on a silicon wafer by magnetron sputtering. The extrapolation of this SIMS erosion rate of pure tin surface to our tin-lithium samples is an approximation motivated by the impossibility of replicating this procedure in a prepared smooth thin film of tin-lithium alloy. It is worth mentioning that this determined erosion rate is a minimum limit value as the expected erosion for Li containing tin layers would be higher due to the smaller binding energy and sputtering threshold of lithium. Notwithstanding, our prepared alloy contains a 98 wt% of tin and additionally after melting the lithium content is supposed to be mainly concentrated on the top surface layers due to the segregation effect [15]. Hence, it seems reasonable to approximate the global alloy erosion rate produced by the SIMS-ToF dual beam for the value obtained for pure tin. For this calibration, a SIMS-ToF depth profile on the reference tin film was carried out. Moreover, the thickness of the tin film and the morphology of the SIMS-ToF crater were measured by stylus profilometry. Fig. 4 shows the results of both measurements. The thickness of the Sn film was estimated around 1400 nm. Considering as criterion that, on the SIMS-ToF profile, the end of the Sn film may be considered as the point where the silicon (substrate) signal reach the 50% of the final value (Si_∞), Fig. 4b shows that the utilized dual beam needed a total time of approximately 3700 s to erode such tin thickness. Consequently, the erosion rate can be estimated as:

$$Y_{SnLi,O_2^+} = \frac{Snthickness}{Sputteringtime} = \frac{1400nm}{3700s} = 0.38nm/s \quad (2)$$

2.3.3. Scanning electron microscope (SEM) and energy Dispersive X-Ray (EDS) analysis

The morphology and composition of the substrate surfaces in contact with the molten alloy was studied by using a Hitachi 4700 scanning electron microscope able to obtain images up to a resolution of few nanometers with a 500000X magnification factor. The instrument also contains a Bruker AXS Quantax 4010 EDS spectrometer able to detect the X-rays emitted by the excited electrons of the top sample surface. When bombarded by the accelerated electron beam of the microscope, characteristic X-rays are emitted that are specific to each element. Such characteristic radiation emitted by the samples is registered by a silicon drift detector and a specific software uses the relative size of the peaks to determine the abundance of the sample elements. Only elements with higher atomic number than beryllium (Z = 4) can be detected, as they contain internal electrons that may produce X-rays due to electron–electron collisions. Consequently, no lithium could be detected during these analyses. Table 1 shows the lines and corresponding energetic levels used for the identification and quantification of the elements present on the different samples. Usually a 20 kV acceleration voltage for the primary beam electrons was utilized in all SEM/EDS measurements.

2.3.4. Laser 3D microscopy

To explore the 3D morphology and topology of the alloy-substrate boundaries a Keyence VK-X1000 3D Laser microscope was used. Although, the instrument is not capable of measuring anything related to elemental composition, it employs a 405 nm laser to map the surface up to a very high resolution (20 nm) imaging and provides excellent 3D profiles in flat, curved and complex surfaces. This proves very useful in observing the nature of the alloy microdroplets-substrate interphases. Additionally, the surface roughness of every substrate was determined with this instrument.

Table 1
X-ray lines and corresponding energy levels used in the EDS quantification.

Element	Sn	Fe	Cr	Ni	Mo	W
Line	L_a	K_a	K_a	K_a	L_a	M_a
Energy Level, keV	3.444	6.405	5.405	7.48	2.292	1.775

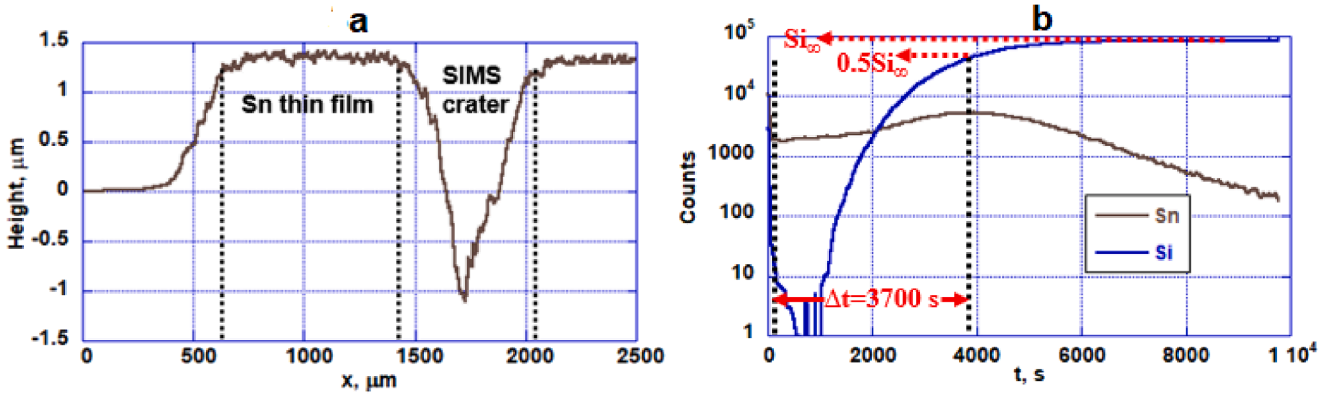

Fig. 4. a) Stylus profilometry scan showing the thickness of the reference thin film of tin and the SIMS crater. b) SIMS analysis showing the depth profile of tin and silicon (substrate), where the total time for the erosion of the tin layer can be inferred for the calibration purposes.

3. Experimental results

3.1. Wetting capabilities of $Sn_{70}Li_{30}$ on 316 SS, molybdenum, and tungsten

The experiments were performed with two different alloy specimens. The first one was employed during the wetting test with 316 SS and tungsten while the second alloy specimen was tested on molybdenum. Based on the bias associated to contact angle determination by MATLAB image tool by different persons, the average experimental error (standard deviation) has been determined for every experimental wetting test. The different error values oscillated between 5 and 2.5 percent (see error bars in Figs. 5–7), being larger for the first performed test (on 316 SS) and decreasing for subsequent test where the deposition of the droplets was optimized, being consequently the shape of the droplets more homogeneous and the determination of contact angle more accurate. In the subsequent plots, the critical wetting value (contact angle of 90°) is represented with a horizontal dashed line while the different established values of wetting temperatures (generally established around the point where subsequent droplets confirm contact angle below 90°) are showed with vertical ones.

Fig. 5 presents the data extracted from the experiments performed on 316 SS. They were collected during three different experimental rounds covering a substrate temperature up to 525 °C. The first test was carried out two weeks after the synthesis of the first alloy specimen. In the data from the first two rounds (with fresh alloy and represented with blue circles) critical wetting is observed from 360 °C (approximate melting point of alloy), with clear decrease in contact angle with temperature. Interestingly, the data from the third round (red squares), where a leftover alloy portion from the second round was kept solid in the injector body under vacuum conditions and then re-melted and studied the next day, systematically shows a clear increase in contact angle. During this last run, the first droplets were deposited at a temperature around 400 °C on the stainless-steel substrate, increasing this temperature for the subsequent droplet depositions. Initially, wetting was observed around 410 °C (vertical dashed line on center). However, in the end of the experiment the droplets, that came from the ultimate portion of the alloy kept re-molten in the injector during around three more hours, needed approximately a temperature of 475 °C to wet. (dashed line on right). All these observations suggest an increase in the wetting temperature from 50 to 120 °C compared to the experiments with fresh alloy, probably revealing the influence of the alloy contamination on its ability to wet substrate surfaces. This shows that long-term utilization of the liquid alloy would be more challenging, requiring higher temperatures to re-start operation.

Tungsten was used as the next material in the experimentation. The results from three experimental rounds are presented in Fig. 6. Observing the data from the first and second rounds with fresh alloy (blue circles) , critical wetting can be considered at a temperature between 405 and 410 °C. This temperature is higher compared to the previously obtained for stainless steel. The third test (red triangles in Fig. 6) explored the behavior of the alloy at temperatures beyond 500 °C. It is important to note that this last round was performed with the final portion of the firstly casted alloy specimen that was synthetized more than 40 days before this utter experiment, also existing a fifteen days gap between this third round and the previous second round on tungsten substrate. During all this time, the alloy was stored in the argon glove box but the results showed a significant increase (100–130 °C) in the necessary temperature for critical wetting, pointing to a influence of the possible long-term contamination of the alloy that would also worsen wettability.

Finally, the works were extended to molybdenum. The tests were performed with a new alloy specimen that was prepared a few days before the first experimental round, being the three rounds performed within a natural week. The obtained data are presented in Fig. 7. Critical wetting can be established around 390 °C, as beyond this value the contact angles were clearly lower than 90°. The measured contact angles presented a general decay with temperature and did not show any drastic increase in subsequent experimental rounds unlike the results presented for 316 SS and tungsten. This opposed behavior seems to be related to the different experimental strategy that determined that, for these tests performed on molybdenum, the alloy was not re-molten or stored during long periods within the globe box. When comparing among the wetting data obtained for the different materials, the specific effect of the surface roughness that varies for every substrate would be coupled to the possible, intrinsic dependence of wetting with material type. Specific experiments varying the surface roughness in every material would be needed to discern the different effects.

During some of the wetting tests, an interesting phenomenon was also visible, involving the sudden gaseous bubbling and related ejection of liquid microparticles (Fig. 8) from the droplets. In such episodes, the droplet surface presented strong passivation with eventual formation of

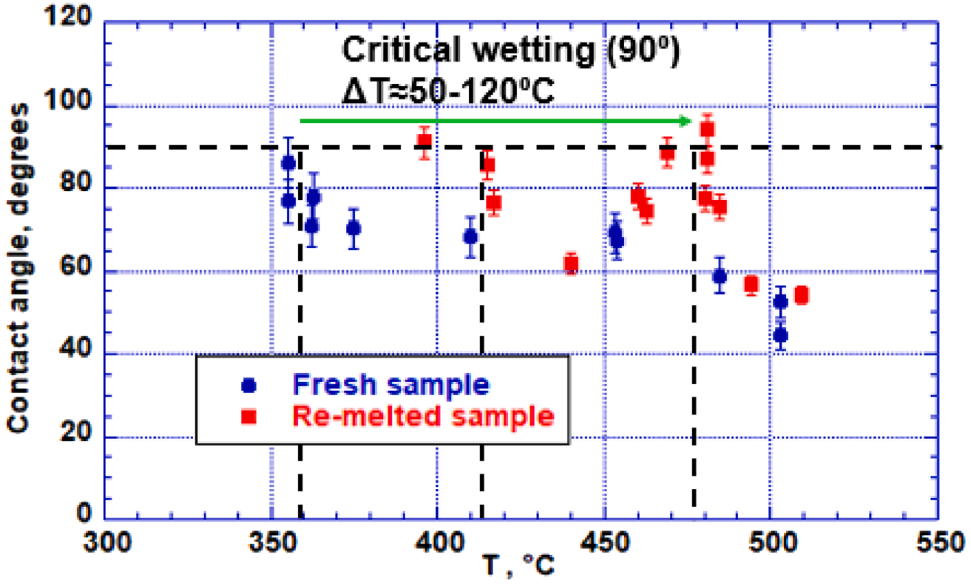

Fig. 5. Wetting data for $Sn_{70}Li_{30}$ alloy extracted from the experiments with 316 SS. Horizontal dashed lines represent critical wetting (contact angle of 90°) and vertical ones the corresponding temperatures for such conditions.

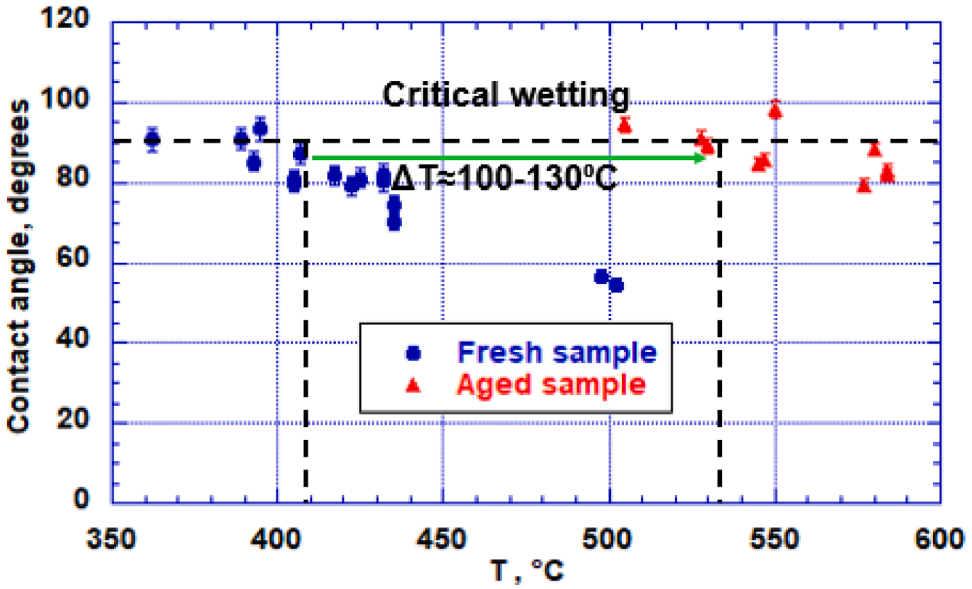

Fig. 6. Experimental data for the wetting test carried out on Tungsten substrate.

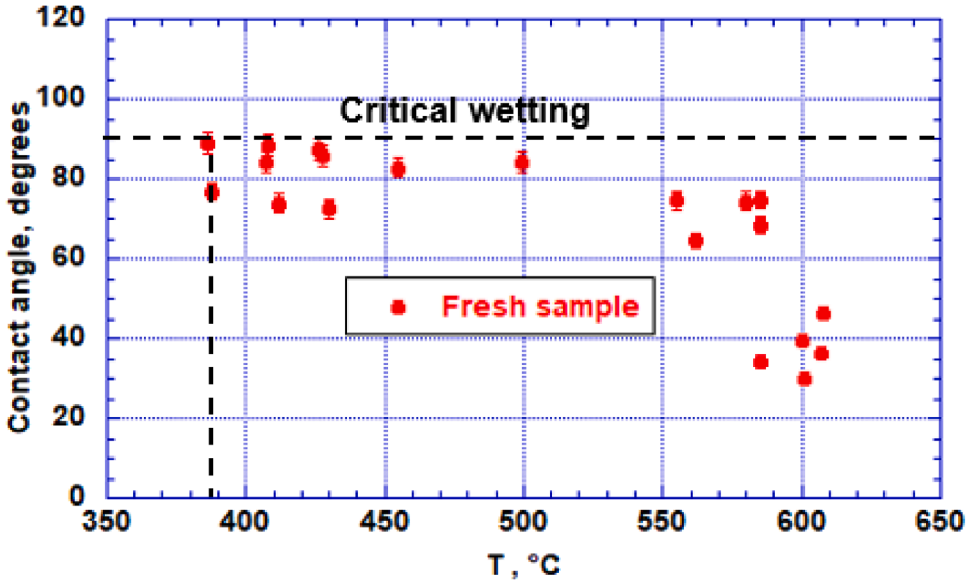

Fig. 7. Contact angles of $Sn_{70}Li_{30}$ droplets deposited on Molybdenum.

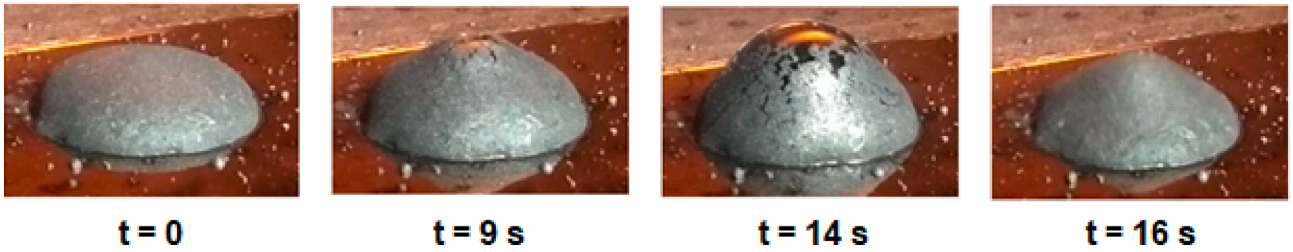

Fig. 8. Sequence of pictures showing the ejection of a gaseous bubble from a SnLi droplet during a wetting experiment performed on 316 SS substrate. Strong passivation can be observed on the surface likely due to Li oxide formation. Due to this ejection, small alloy microdroplets were expelled, being visible on the substrate region adjacent to the main droplet.

crust layers on droplet top surface that was clearly visible. These events happened over a wide range of surface temperatures (400-500ºC). It is worth mentioning that this ejection phenomenon appeared to be more frequent when size of the droplets was bigger as a consequence of a deficient deposition/injection of the liquid metal. Such droplets were not utilized for the wetting data determination. Additionally, this

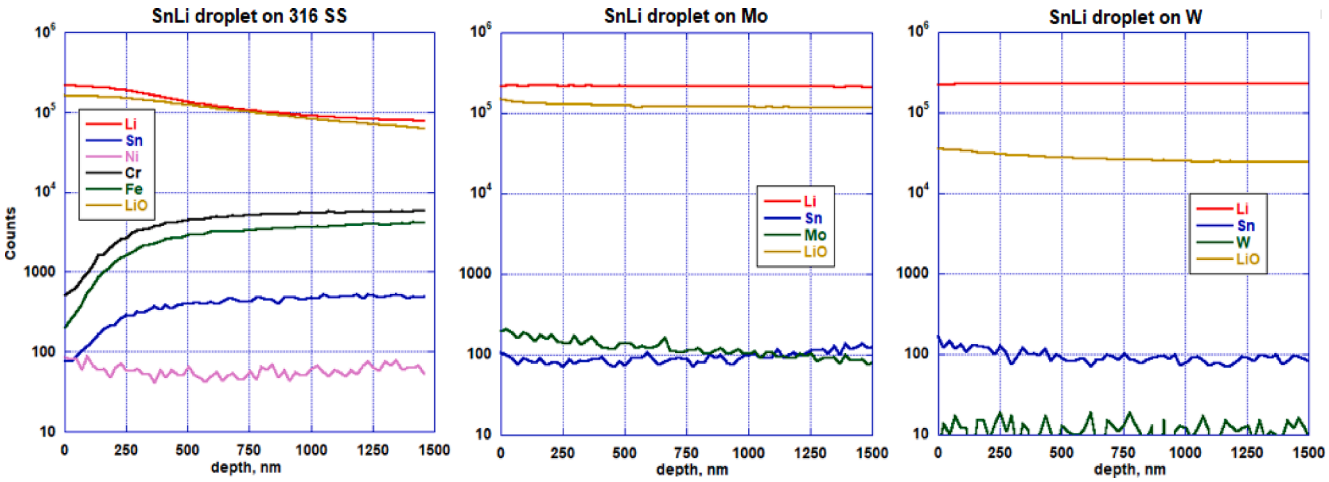

Fig. 9. SIMS profiles for SnLi droplets deposited on 316 SS (left), Mo (center) and W (right).

ejection was more accentuated in the case of 316 SS substrate (material that was in contact with the alloy during the episode showed in Fig. 8), being perhaps partially influenced by a stronger material mixing with this substrate. Although the specific causes of these observations are uncertain, perhaps the ejection could be related to sudden preferential evaporation of lithium from the droplets or depletion of gaseous impurities stored in the liquid alloy bulk. This shows concerns about the stability of the $Sn_{70}Li_{30}$ liquid alloy. Related to this phenomenology, the alloy microdroplets (created by the bubble ejection and visible in Fig. 8) produced changes in the color and general appearance of the substrate. These findings were studied at the microscale by post-mortem techniques (see results of Section 3.2.3)

3.2. Post-mortem characterization of studied elements

3.2.1. Tin-lithium alloy composition determination

The results of the ICP-OES analyses are presented in Table 2. They show the composition of different portions of the alloy, including previously molten portions originally investigated as droplets during the wetting experiments (samples named as SnLi2, SnLi3 and SnLi4) as well as one specimen directly taken from the synthetized first alloy (named as SnLi1). Generally, the total mass of the analyzed specimens was around 200–300 mg. The analyzed molten droplets belonged to the two different synthetized alloy specimens (SnLi1, SnLi2 and SnLi3 came from the first specimen, while SnLi4 corresponds to the second one) prepared during different casting rounds, but with the same original desired Sn/Li proportion (global composition $Sn_{70}Li_{30}$).

The composition of all samples was quite similar compared to the composition of the original desired mixture ($Sn_{70}Li_{30}$). The samples experimented as droplets during the wetting test presented a composition with a higher concentration of tin. In this way, the exposure at liquid state during the experiment appeared to reduce lithium content of the alloy. On the other hand, comparing all the previously deposited samples that were obtained after the wetting experiment on the different substrate materials, they presented minuscule differences in composition. The different origin (two different synthetized alloys) of these samples shows the good reproducibility of the synthesis process. Finally, the proportion of impurities deduced from the Sn and Li quantification showed an expected accumulation of impurities with time. The residual content (that balances wt. % to a value of a hundred) not detected as Li or Sn was drastically reduced for the case of the non-deposited sample (SnLi1). This specimen was analyzed before any melting or experimental exposure, being stored in inert/dry air conditions inside the glovebox for proper preservation only during a few days before being sent to ICP-OES measurements. Consequently, its purity appeared significantly higher, presenting a very small residual impurity content of 0.04 wt%, which is two orders of magnitude lower compared to the other three samples. Such a considerable difference was produced by the accumulation of impurities due to the passivation of these samples during the wetting experiment, as well as the longer exposure to the atmosphere until the ICP-OES quantification.

Table 2
ICP-OES quantification in the SnLi samples.

Sample	Nature	Substrate (wetting test)	Sn (wt. %)	Li (wt. %)	Composition (subscrit≡at. %)
SnLi1 1st alloy	Casted portion	None	97.00	2.96	$Li_{34.4\pm1.0}Sn_{65.6\pm 1.0}$
SnLi2 1st alloy	Molten droplet	Stainless Steel	96.35	2.16	$Li_{27.7\pm1.0}Sn_{72.3\pm1.0}$
SnLi3 1st alloy	Molten droplet	Tungsten	94.95	2.13	$Li_{27.7\pm1.5}Sn_{72.3\pm1.5}$
SnLi4 2nd alloy	Molten droplet	Molybdenum	94.70	2.04	$Li_{27.2\pm1.2}Sn_{72.8\pm1.2}$

3.2.2. SIMS-ToF depth profiles on alloy and substrates

The base (flat) side of three alloy droplets deposited on the different substrates, as well as the substrate surfaces showing alloy microparticles (Figs. 10 and 13) were analyzed with SIMS-ToF. Analysis was attempted on the curved (semispherical face not in contact with the substrate) part of the droplet but the presence of insulating passivated layers precluded the transference of energy from the ion beam to the surface species. Consequently, no coherent flux of secondary sputtered ions was detected. The absence of proper standards did not allow the absolute

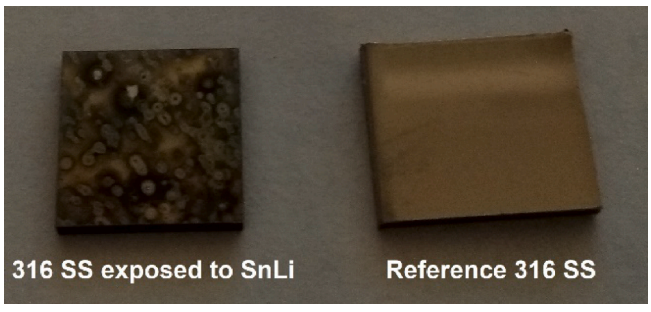

Fig. 10. Specimens of 316 SS substrate analyzed by SIMS-ToF.

quantification of the elemental composition along the depth profile. Therefore, the different elemental signals cannot be directly compared as their values depend on the ease of each element to be sputtered, ionized, and finally detected by the instrument. For this reason, although the absolute amount of lithium present in the alloy is much smaller compared to tin, it shows a larger SIMS-ToF signal. Ultimately, the detected signals depend on relative sensitivity factors (RSF) that are specific to each element [36]. Roughly, in the case of O_2^+ beam analysis, lithium presents a signal three orders of magnitude higher than tungsten signal, two order of magnitude higher than molybdenum, nickel (Ni), iron (Fe) and tin ones and around one order of magnitude higher than chromium (Cr). Additionally, the observation of the temporal evolutions of the signals, their normalization, and the comparison of the same element signals between different samples can be useful for relative semi-quantification and/or qualitative characterization.

The results obtained from the base flat surface of the three $Sn_{70}Li_{30}$ droplets are shown in Fig. 9. On all samples, the lithium signal (^{7}Li isotope) appears in the range of $2\text{-}3\cdot10^5$ showing appreciable changes with depth in the case of the droplet deposited on 316 SS, with higher amount of lithium closer to the surface. Nonetheless, possible lithium segregation to the surface should not be specific to the substrate in which the droplet was deposited and, according to theory, should appear only in the range of few tens of nm deep. All the lithium signals are accompanied by a comparable signal of (LiO). Such stoichiometry may represent a global mixture of lithium oxide, peroxide and superoxide present on the sample layers due to oxidation of original lithium content or otherwise might be produced by the bombardment with the oxygen beam during the depth profile analysis. In any case its presence is totally associated to lithium with frequent parallel signal to it. Larger tin values are also present for the droplet deposited on 316 SS, showing an increasing profile with depth that is also visible (parallel signals to tin one) in the steel constituents (chromium and iron). Such gradient in the tin content exceeds the penetration depth (few nm) where lithium segregation effects are supposed to happen, showing perhaps some phase separation in the alloy extended to the range of hundreds of monolayers (up to 500 nm of depth). On the other hand, the incorporation of 316 SS constituents into the tin matrix took place after an exposure no longer than 3 h, which was the maximum duration of the wetting experiments in stainless steel at temperatures < 550 °C.

On the contrary in the case of W or Mo, their signals are much lower and without any gradient in depth, thus indicating a much weaker or even nonexistent (for the case of tungsten the corresponding signal is clearly in the range of the background noise) interaction with the alloy constituents. Considering that Mo detection by SIMS may be generally expected as one order of magnitude higher compared to tungsten [36], one can infer that the subsequent Mo signal may be at the same approximate level (background noise) compared to the tungsten one. Regarding the oxide impurities of lithium, alternative depth profile analysis using the Cs^+ beam also showed high presence of Li oxide impurities hence confirming that the LiO signals visible on Fig. 9 cannot be attributed to the effects of the O_2^+ beam, being mainly produced by the surface passivation processes of the lithium layers.

On the other hand, substrate surfaces (Figs. 10 and 13) that were in contract with alloy microparticles were also analyzed with the results present in Figs. 11 and 14. For the 316 SS substrate exposed to the alloy, the shape of lithium and chromium (Cr) profiles appears very similar. On layers situated deeper than the sample surface (signal values recorded at a time around 500–600 s), there is a peak in the value of both lithium and chromium signals that is almost coincident. This observation indicates the penetration of lithium in the 316 SS matrix. Fig. 12 shows the normalization (dividing by their maximum values) of the commented profiles, showing that they are essentially coincident and indicating that the interaction of the alloy with the steel matrix was able to deplete chromium. Previous research has shown that corrosion induced by liquid lithium on stainless steel is characterized by this lithium penetration and chromium depletion with formation of complex Li-Cr compounds [37]. This result indicates that first evidence of lithium induced corrosion can be observed after short exposures to the liquid $Sn_{70}Li_{30}$ alloy at temperatures < 550 °C. Equivalent measurements were performed on molybdenum and tungsten substrates. Such samples are shown (together with reference ones) in Fig. 13, where the presence of small alloy microparticles surrounded by a surface with color changes is also visible. Fig. 14 shows the corresponding depth profiles. Although the alloy constituents are present in the obtained depth profiles, considering the previously general RSF values for detection, such signals really correspond to very low concentrations compared to molybdenum and tungsten, also presenting an extremely rapid drop non-associated to the corresponding substrates. Consequently, it seems clear that presence

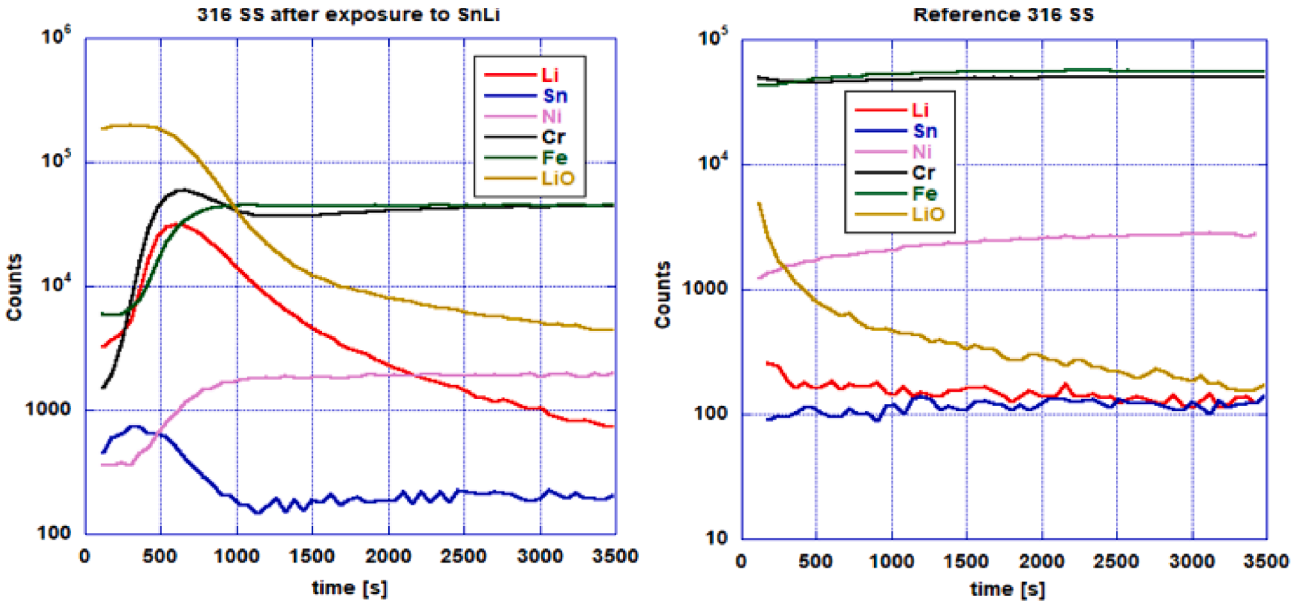

Fig. 11. SIMS ToF profiles on 316 SS exposed to SnLi (left) and reference 316 SS (right). Signals of Li, LiO and Sn (red, yellow and blue respectively) in the reference sample (right) are well below (and order of magnitude) those corresponding to the sample that really contained the commented elements. This contamination likely relies on the unavoidable presence of residuals in the SIMS analyses chamber and may be used as the reference for the background of such signals.

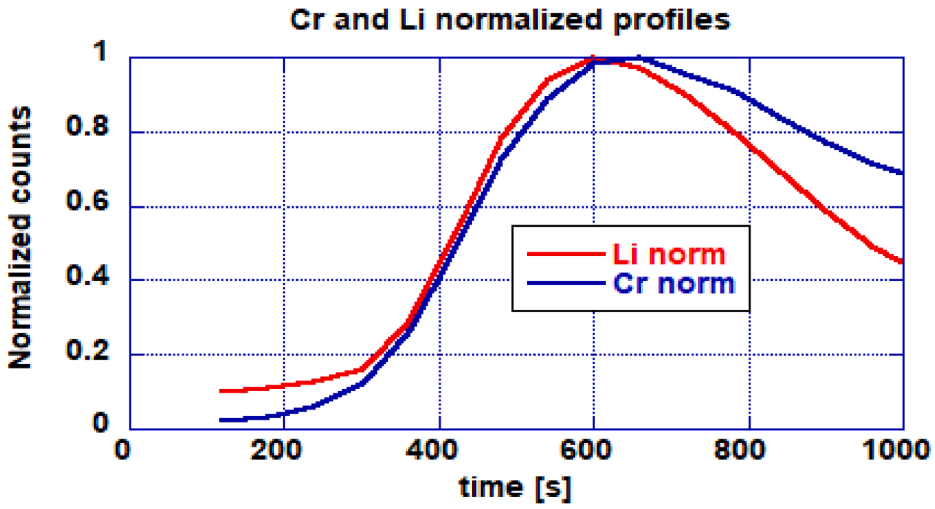

Fig. 12. Normalized profiles of Cr and Li present on previous 316 SS sample. The coincident profiles are a sign of Cr and Li association in the substrate because of the interaction with the alloy.

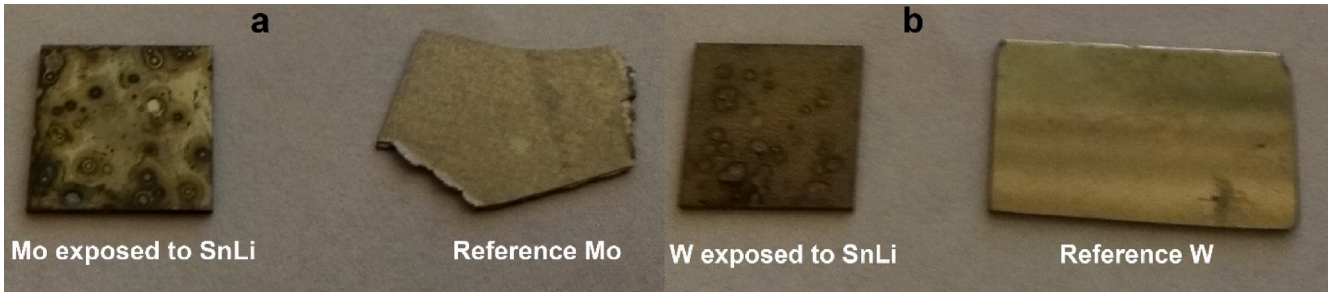

Fig. 13. Molybdenum samples (a) and tungsten ones (b) analyzed by SIMS-TOF.

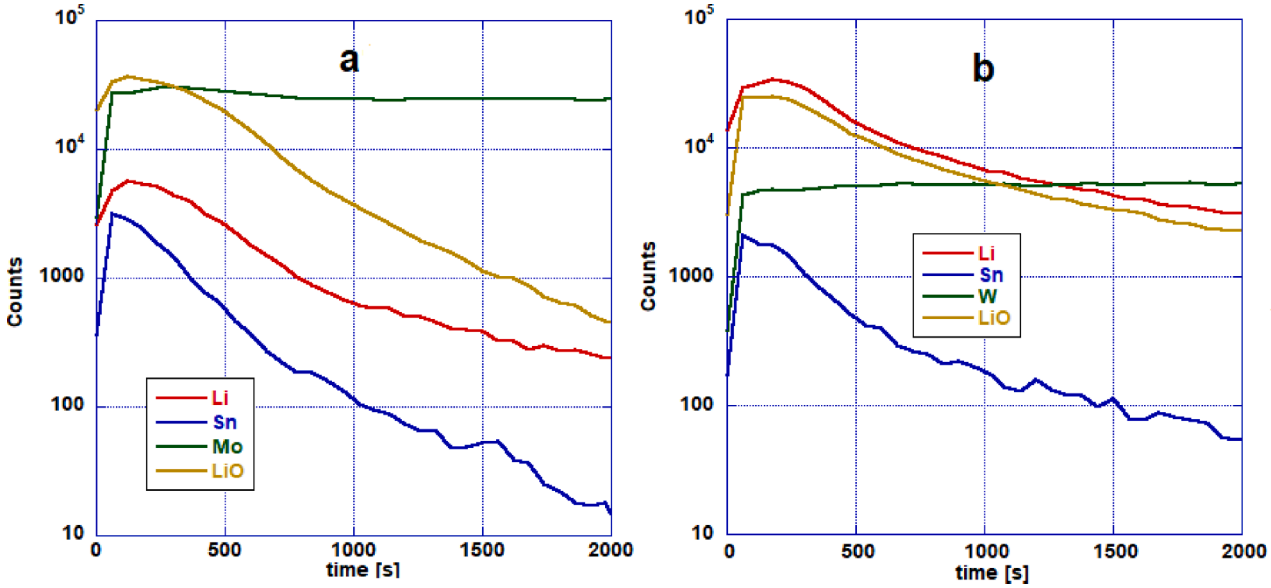

Fig. 14. SIMS-ToF depth profiles on molybdenum (a) and tungsten (b) exposed to $Sn_{70}Li_{30}$.

of the alloy elements is restricted to the top surface, with no signs of tin/lithium penetration/diffusion and/or association with substrates.

3.2.3. SEM-EDS performed on tin-lithium microdroplets present on substrates and associated 3D laser microscopy analyses

SEM pictures were collected showing details about the morphology and microstructure for the case of three different alloy microparticles present on 316 SS, molybdenum, and tungsten. EDS was utilized to quantify the elemental composition in different regions of the analyzed system, covering microdroplet, substrate, and the mutual boundaries. Fig. 15 shows the results for all studied materials. The alloy microparticles presented a size around 100 μm in the major dimension. The red

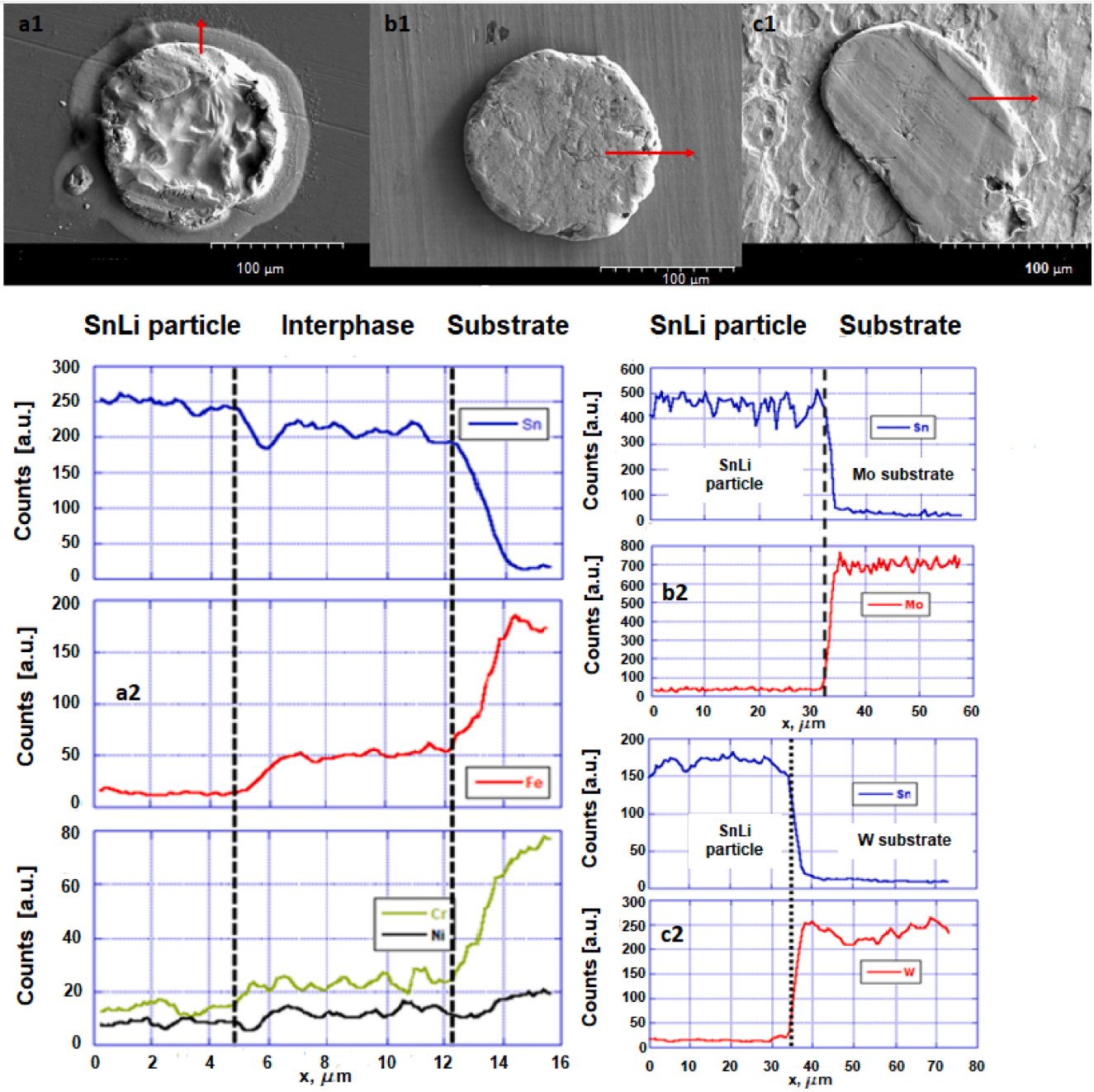

Fig. 15. Morphology of SnLi microparticles (SEM images identified as a1, b1, c1 subplots) and corresponding linear EDS profiles showing elemental* composition for 316 SS substrate (a2), Molybdenum (b2) and Tungsten (c2**).** *Note that lithium cannot be detected by EDS.

arrows represent a linear direction along which the EDS scan was performed to determine the relative presence of the components on the top surface of the different regions. In the case of 316 SS substrate, the boundaries surrounding the particle present a mixing interphase that is not present on the other two substrates. Furthermore, the EDS radial profiles also reveal that this intermediate region between the microparticle and the 316 SS substrate is characterized by a progressive change in the element signals. For the other two cases (molybdenum and tungsten) the change in the corresponding signals is much more drastic presenting an abrupt profile between the substrate and alloy microparticle, thus corroborating the absence of mixing between them. Additionally, absolute quantification of the composition was performed by EDS in several points of the top surface of each region for the three different substrate-microparticle pairs. Interestingly, for the case of the mixing interphase observed in the 316 SS substrate, the averaged results of these quantifications revealed a Sn/Fe atomic ratio of 1.0 ± 0.4 on the surface of this region that agrees with a stoichiometry corresponding to intermetallic iron stannide compounds (FeSn and $FeSn_2$). The corresponding obtained Sn/Ni and Sn/Cr ratios on this region were 3.0 ± 1.1 and 8.4 ± 1.4, showing lower 316 SS constituent contents compared to iron ones. Previous works have shown that formation of iron stannides (alloy type corrosion) dominates the overall attack of liquid tin on austenitic steels like 316 SS at temperatures below 700 °C [38]. Although, nickel leaching has been also found to be present (at lower scale) at this temperature level. For molybdenum and tungsten, however, the same liquid–solid interaction did not produce any equivalent mixing or attack. The registered Sn/Mo and Sn/W ratios on the surface of the substrate-alloy boundaries were clearly below 0.02, values that

cannot be really distinguished from the experimental error associated to the EDS quantification. This result corroborates the compatibility of molybdenum and tungsten with the alloy. On the contrary, these results indicate that first signs of tin induced corrosion are already visible on 316 SS after a short exposure to the liquid $Sn_{70}Li_{30}$ alloy. It may be argued that the substrate signals detected by EDS in the mixing interphases may be originated on the substrate bulk present beneath. This situation would happen if the penetration depth of the utilized electrons is larger than the height of the studied mixing boundaries. Using, the equation derived from Everhart and Hoff [39], the penetration depth of the electron beam may be estimated as:

$$\delta = \frac{0.04E^{1.75}}{\rho}\mu\text{m} \quad (3)$$

where E is the acceleration voltage in keV (20 in our case) and ρ, the density of the studied substrate in g/cm^3. Considering the equimolar Fe-Sn layer, measured by EDS, as the majority component of the mixing boundary, with average density of 7.49 g/cm3, a value around 1.0 μm is obtained for the electron penetration depth.

The height and morphology of the mixing boundaries for the three substrates was analyzed by 3D laser microscopy, (Fig. 16). As Fig. 16a shows, the height of the 316 SS-SnLi mixing boundaries (dashed oval) may be established around 10 μm when compared to an adjacent portion of substrate where no alloy is present (continuous line circle). Such height value is clearly beyond the electron penetration depth; hence the previous results are representing the real composition of the mixing boundaries object of study. Fig. 16c and 16d show the corresponding 3D profiles of alloy microparticles present on Mo and W respectively. They corroborate the absence of equivalent interaction with the alloy compared to the case of 316 SS substrate.

4. Discussion and implications for tin-lithium alloys utilization in flowing liquid metal PFCs

Considering that tin-lithium alloys are envisioned as a potential replacement for lithium, at this point it is interesting to make a global comparison between both liquid metal options in terms of wetting capabilities. The specific experiments with lithium [25] showed approximated wetting temperatures around 315 °C, 325 °C and 350 °C for stainless steel, molybdenum and tungsten respectively while the corresponding values here reported are around 360 °C, 390 °C and 405 °C for the fresh $Sn_{70}Li_{30}$ alloy. Such values are only 45–55 °C higher that those corresponding to lithium and does not suggest a large increase with respect to the melting point of the alloy (around 360 °C). Although an intrinsic influence of the higher roughness of the utilized molybdenum and tungsten substrates is expected, some substrate dependence of the wetting temperature seems to follow the same trend compared to the wetting behavior of lithium. In this way, $Sn_{70}Li_{30}$ alloy also seems to wet better (i.e. at lower temperature) 316 SS and molybdenum, needing a higher temperature to wet tungsten. In practice, the most important observation reflects that if the alloy is sufficiently well-preserved, it wets a mirror finished 316 SS substrate as soon as it melts and commercial roughness molybdenum and tungsten at slightly higher temperatures. In contrast, preliminary trials (limited to only few droplets), performed with $Sn_{80}Li_{20}$ alloy [40] and pure tin [41], clearly showed non wetting characteristics (large contact angles beyond 115°) up to temperatures of 410 °C ($Sn_{80}Li_{20}$ on commercial 304 SS), 435 °C ($Sn_{80}Li_{20}$ on rough W) and 500 °C (pure tin on mirror finished 316 SS). Considering that these materials have melting points lower that the $Sn_{70}Li_{30}$ alloy (232 °C for tin and around 320 °C for $Sn_{80}Li_{20}$), this comparison might suggest better wetting capabilities for alloys containing higher lithium (whose surface tension is lower compared to tin) proportion possibly segregated into the surface that, in this case, could dominate the wetting process.

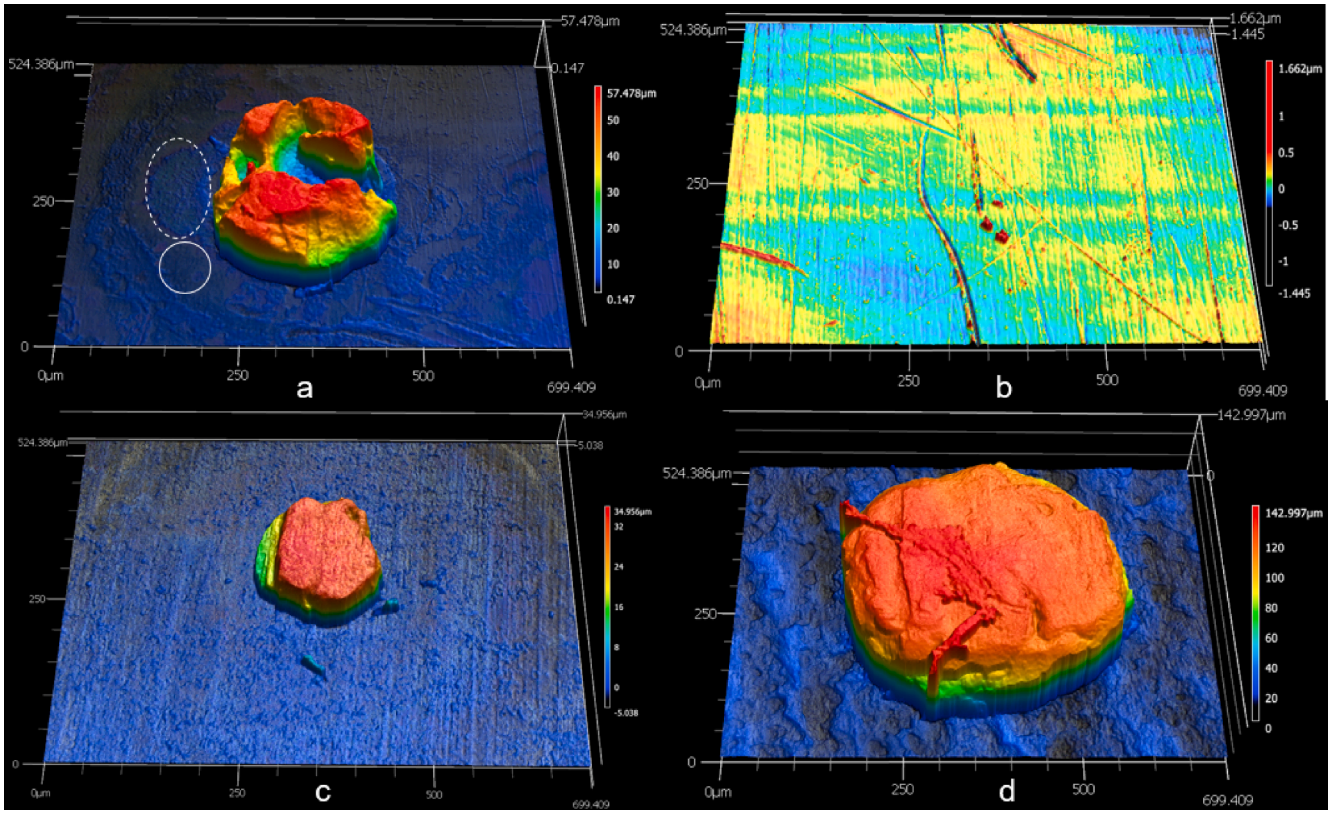

Fig. 16. 3D Laser microscopy measurements on SnLi microparticles deposited on 316 SS (a), molybdenum (c) and tungsten (d). Fig. 16 b shows a measurement performed on a reference 316 SS substrate where no alloy was deposited. Dashed oval represents a 316 SS-SnLi mixing layer and continuous line circle an adjacent portion of substrate where no alloy is present.

These results represent the first observations of proper wetting of tin-lithium alloys at moderate temperatures that bode well for potential and realistic flowing liquid metal PFC scenarios. Additionally, surface roughness effect on wetting is unarguably present, then more detail and specific studies for each material are necessary to distinguish and assess such multiparametric dependence. These studies would be also important to determine a compromise between surface roughness/morphology for wetting, but also considering the stability of LM regarding jxB forces. In such environment, rougher CPS structures have demonstrated to add capillary force for liquid surface stabilization against ejections and dryout [42], but on the contrary, may complicate the wetting process.

Nevertheless, the wetting properties of the studied alloy seems to be significantly dependent on the alloy status. Two forms of contamination might affect the wettability. Firstly, the passivation of the alloy when maintained liquid in vacuum conditions (from $2{\cdot}10^{-5}$ to $5{\cdot}10^{-6}$ Torr) at time scales of hours within an experimental test or after solidification of liquid alloy leftovers during timescales of one day. This is the case of the data collected during the last test performed on 316 SS (red squares in Fig. 5) that showed a quite significant increase in the wetting temperature (up to 120 °C). The second form is the contamination of the prepared alloy during its storage in the inert argon/dry air glovebox. This is the situation that could explain the abnormal results obtained during the last experimental round performed with the tungsten substrate, when the final portion of the casted alloy was utilized after more than 40 days from its casting. Such circumstance appears to affect the wetting capabilities of the alloy on tungsten, increasing the necessary temperature by up to 130 °C as is shown in Fig. 6. This temperature increase would determine direct technological issues (higher heating requirements), potential problems in the alloy stability, and related evaporation as well as a worsening of potential corrosion problems that would be enhanced with temperature. None of these deleterious effects were observed for the molybdenum testing, where the experimental procedure avoided this residual vacuum and/or long-term contamination of the alloy during its glove box preservation. Concerning this second contamination source, the utilized preservation protocol of lithium compounds after any glove box opening establishes previous and posterior argon flow (20–30 min length) throughout the storage volume, to remove atmospheric gases. After it, for economic reasons, the glove box is continuously vented with dry air while the lithium compounds are stored in the glove box. Such water free environment is known to be the key to slow lithium passivation [43]. Notwithstanding, even this preservation conditions could produce exposition to small concentrations of water, thus likely inducing slow contamination that would be obviously increased with storage time. To reduce this deleterious effect, some actions as a more accurate monitoring of water content inside the glove box, a better water absorption protocol within it and the improving of the sealing and preservation of the alloy inside better containers (perhaps totally covering specimens with liquid paraffin) seems especially recommendable. Besides that, for operation re-start in experimental devices, the use of cryopumping units to reduce the base pressure inside vessel during and/or among experiments will undoubtedly help.

Another important observation is related to the liquid stability of the alloy. The gaseous bubbling and ejection from liquid droplets could be problematic in a real fusion device environment as it is a source of deleterious high Z impurities for the plasma. The observations point to a reduced homogeneity and stability of the investigated alloy mixture that perhaps may be affected by preferential evaporation of lithium and/or phase separation, even producing partial decomposition. The studied alloy composition lies in between two eutectic/eutectoid points ($Sn_{43}Li_{57}$ and $Sn_{95}Li_5$ [35]) and consequently its long-term stability and homogeneity may not be optimal. The strong segregation of lithium into the surface, that characterizes the alloy, leads to preferential sputtering of the light element [16]. This fact that may suppose the potential exposition of a rich tin rich surface facing the plasma after a given operational time. It would entail direct issues associated to high Z impurity contamination if the lithium content on the surface is not reconstituted, thus appearing more problematic for CPS solutions where replenishment is not macroscopic. On the other hand little is known about the potential role of this segregation in the possible preferential evaporation of lithium that may cause a similar problem. The results of the post-mortem ICP-OES analyses here presented show that the lithium content of the alloy decreases after its employment in liquid state during the wetting experiments, perhaps suggesting that this preferential evaporation could, indeed, happen.

The impurity/hydrogen gettering and related passivation can also affect the commented liquid homogeneity/stability. Molecular dynamic simulations performed with $Sn_{70}Li_{30}$ [44] alloy have shown that the interaction of the liquid alloy with deuterium could produce the trapping of gaseous particles that may lead to their eventual bubble release due to the low affinity of the internal tin-lithium structure by hydrogenic species. Likewise, such droplet ejection has been recently observed from both free surface and CPS liquid tin samples exposed to linear deuterium plasmas [45]. The phenomenon seemed to be associated to the presence of cavities in the liquid tin bulk where its low hydrogenic retained inventory may be accumulated in gaseous bubbles that eventually burst. Although our liquid alloy droplets were not exposed to deuterium, this unstable accumulation of gaseous species in liquid tin-based materials could play a role in the observed ejection episodes if this prediction is somehow equivalent or similar for the case of nitrogen, oxygen or another residual gases. In addition, such impurity accumulation on the alloy, and its eventual release might enhance inhomogeneity in the liquid structure, also favoring phase separation and/or alloy decomposition and, more importantly, act as a high Z source for the plasma. To ameliorate these issues, operation with real eutectic/eutectoid compositions that, in principle, are expected to be more stable, seems a logical continuation of the experimental endeavors, in order to find a more suitable scenario where the free surface stability and flow of the alloy can be favored. In this respect, while the $Sn_{95}Li_5$ eutectic presents a lower melting point (222 °C [35]), its low amount of lithium may not be beneficial from a plasma compatibility point of view. Additionally, as previously discussed, lower lithium content in the alloy might be associated to more challenging wetting. The situation with the $Sn_{43}Li_{57}$ eutectoid would be the opposite as it presents a considerably higher melting point (470 °C [35]) but, at the same time, much larger lithium content. While it will obviously imply a higher minimum temperature requirement for primary melting, in the case of a hypothetical power plant, such circumstance would be associated to more efficient electrical conversion [46]. The higher lithium content might, likewise, help in the necessary wetting behavior.

Finally, regarding material compatibility, our experiments have corroborated the expected corrosion behavior between the alloy and 316 SS. At moderate temperature, the $Sn_{70}Li_{30}$ alloy only needed a short time (around three hours) to attack the steel substrate at the microscale forming an alloyed interphase layer of Fe-Sn compounds. SIMS-ToF results also show that lithium can penetrate the steel matrix and interact with chromium at this time scale. On JLF-1 and 316 steels the previous experiments of Kondo et al., with $Sn_{80}Li_{20}$ alloy during much longer timescales (250 and 750 h) [34] basically reported the same corrosion pattern induced by liquid tin, although no signs of lithium and chromium association were reported. The results here reported suggest that the corrosion problem between tin-lithium alloys and 316 SS can include chromium leaching induced by lithium. Such corrosion on the substrate might be expected to affect the wetting pattern as well. First, the process will gradually change the composition and properties of the solid iin contact with the liquid alloy. Secondly, the contamination of the alloy with substrate and residual vacuum constituents will be present as well, thus interacting in the wetting process that happens in the interface. In our experiments the wetting process is measured immediately after the deposition of the liquid metal with the substrate, well before any corrosion sign can be present (first tens of seconds). In this way, any possible effect of such processes in the investigated droplets may be

discarded. Nevertheless, in a much longer-term operation, as foreseen in a relevant fusion experiment such effects would be unavoidable. Therefore, the use of 316 SS in combination with the studied alloy in flowing liquid metal components appears extremely problematic as in these configurations a more notorious degradation can be expected as a result of the dynamic effects and the friction induced by macroscopic liquid metal flow. Operation with molybdenum or tungsten seems much more plausible from this point of view, but also may favor tin-lithium flow due to their larger Seebeck coefficient (respect to liquid tin) compared to stainless steel and the related Thermoelectric Magnetohydrodynamic effects [47]. Nonetheless, the more laborious machining of these materials compared to stainless steel may require more sophisticated methods (such as 3D printing) for advanced and geometrically complex PFC manufacturing [42,48].

5. Conclusions and future works

The first wetting characteristics of $Sn_{70}Li_{30}$ have been obtained on 316 SS, molybdenum, and tungsten substrates. The alloy status and its contamination were found to impact the results. While the fresh, non-contaminated alloy showed wetting at temperatures around 360 °C-405 °C, the contamination of the alloy seemed to increase the values by 120–130 °C.

Additionally, a complete characterization of $Sn_{70}Li_{30}$ alloy was carried out by a multi-technique approach. ICP-OES absolutely quantified the alloy specimens, corroborating a $Sn_{70}Li_{30}$ composition and the reproducibility of the synthesis process. SIMS-ToF depth profiles were determined on alloy droplets and also in 316 SS, Mo, and W substrates that were in contact with the liquid alloy. SEM/EDS and 3D laser microscopy enabled deeper study of the corrosion pattern produced on 316 SS. Interestingly, future works with alloys presenting different Li/Sn composition may open the possibility of cross-checking the ICP-OES and SIMS-ToF results. Such comparison may enable a possible absolute calibration method for the SIMS-ToF technique in terms of Li/Sn content along the depth profile.

The SIMS-ToF analyses performed on an alloy droplet deposited on 316 SS have shown the incorporation of steel components (iron and chromium) into the alloy. Alternative analysis performed on 316 SS substrate presenting alloy leftovers also indicated the first evidence of lithium induced corrosion (chromium depletion and association to lithium) while Mo and W did not show any association to the alloy constituents. SEM/EDS and 3D Laser microscopy results showed mixing boundaries between 316 SS and alloy microparticles with a stoichiometry compatible with iron stannide formation that characterizes liquid tin induced attack (alloying type corrosion). Equivalent analysis did not show any of these corrosion signs on W and Mo.

These results indicate that both lithium and tin-induced corrosion may be present on 316 stainless steel exposed to $Sn_{70}Li_{30}$ at small timescales and moderate temperatures ($t \leq 3$ h, $T < 550$ °C). The rapid material attack and the non-compatibility of the alloy with 316 SS discourage the use of this substrate even for preliminary testing at laboratory scale. As expected, molybdenum and tungsten showed a different behavior. There were no signs of mixing between alloy and substrate at the microscale, nor association between alloy elements and substrates after equivalent contact with the liquid alloy. Thus, this encourages any future testing with tin-lithium alloys in flowing liquid metal components to be carried out on tungsten and/or molybdenum-based materials. Finally, sudden ejection of gaseous bubbles from liquid alloy droplets was observed, thus revealing constraints related to the stability of the $Sn_{70}Li_{30}$ alloy as a homogenous liquid entity.

Further experimentation will be centered in the eutectic/eutectoid compositions ($Sn_{95}Li_5$ /$Sn_{43}Li_{57}$) in order to find the best possible scenario (alloy composition, liquid stability, temperature window and related wetting conditions) for the eventual utilization of tin-lithium alloys in flowing liquid metal PFCs. In this sense, additional studies regarding: possible preferential evaporation of lithium, vapor pressure characteristics of the alloy and related effects in its stability, temperature operational window as well as specific dynamic erosion/corrosion experiments with molybdenum and tungsten also appear worthwhile for this global task.

CRediT authorship contribution statement

A. de Castro: Conceptualization, Data Curation, Formal analysis, Investigation, Methodology, Software, Validation, Visualization, Writing-original draft, Writing-review & editing. **C. Moynihan:** Conceptualization, Investigation, Methodology, Software, Writing-review & editing. **S. Stemmley:** Conceptualization, Investigation, Methodology, Software, Writing-review & editing. **M. Szott:** Conceptualization, Investigation, Methodology, Writing-review & editing. **D. Andruczyk:** Conceptualization, Project administration, Resources, Supervision. **D. N. Ruzic:** Conceptualization, Funding acquisition, Project administration, Resources, Supervision, Writing-review & editing.

Declaration of Competing Interest

The authors declare that they have no known competing financial interests or personal relationships that could have appeared to influence the work reported in this paper.

Acknowledgments

This work was supported by USA Department of Energy/ALPS contract: DEFG02-99ER54515.

The authors want to recognize the valuable help of Dr. T. Spila during the realization of the SIMS-ToF analyses and acknowledge Dr. K. Subedi that carried out the ICP-OES measurements in the Microanalysis Laboratory of the University of Illinois.

This work was carried out in part in the Frederik Seitz Materials Research Laboratory, Central Research Facilities, University of Illinois.

References

[1] A. Kallenbach, M. Bernert, R. Dux, et al., Impurity seeding for tokamak power exhaust: from present devices via iter to demo, Plasma Phys. Controlled Fusion 55 (2013), 124041.
[2] G. Matthews, B. Bazylev, A. Baron-Wiechec, et al., Melt damage to the JET ITER-like wall and divertor, Phys. Scr. T167 (2016), 014070.
[3] S. Entler, J. Horacek, T. Dlouhy, et al., Approximation to the cost of fusion energy, Energy 152 (2018) 489–497.
[4] R.E. Nygren, F.L. Tabares, Liquid surfaces for fusion plasma facing components-A critical review. Part I: Physics and PSI, Nucl. Mater. Energy 9 (2016) 6–21.
[5] A. Loarte, B. Lipschultz, A. Kukushkin et al., Chapter 4: Power and particle control, Nucl. Fusion, 47, (2007) S203-S263.
[6] R. Majeski, R. Doerner, T. Gray, et al., Enhanced energy confinement and performance in a low-recycling tokamak, Phys. Rev. Lett. 97 (2006), 075002.
[7] R. Maingi, D.P. Boyle, J.M. Canik, et al., The effect of progressively increasing lithium coatings on plasma discharge characteristics, transport, edge profiles and ELM stability in the national spherical torus experiment, Nucl. Fusion 52 (2012), 083001.
[8] J.S. Hu, Z. Sun, H.Y. Huo, et al., "New steady-state quiescent high confinement plasma in an experimental advanced superconducting tokamak" Phys, Rev. Lett. 114 (2015), 055001.
[9] D.P. Boyle, R. Majeski, J.C. Schmitt, et al., Observation of flat electron temperature profiles in the lithium Tokamak experiment, Phys. Rev. Lett. 159 (2017), 015001.
[10] L.E. Zakharov, On a burning plasma low recycling regime with p DT = 23–26 MW, q DT = 5–7 in a JET-like tokamak, Nucl. Fusion 59 (2019), 096008.
[11] M. Poradzinski, I. Ivanova-Stanik, G. Pelka, et al., Integrated power exhaust modelling for DEMO with lithium divertor, Fus. Eng. Des. 146 (2019) 1500–1504.
[12] M.P. Christenson, The Design and Development of Hydrogen Isotope Extraction Technologies for a Limit-Style Liquid LITHIUM Loop, PhD thesis, University of Illinois at Urbana-Champaign, 2018.
[13] M. Ono, R. Majeski, M.A. Jaworski, et al., Liquid lithium loop system to solve challenging technology issues for fusion power plant, Nucl. Fusion 57 (2017), 116056.
[14] M.A. Abdou, A. Ying, N. Morley, et al., On the exploration of innovative concepts for fusion chamber technology, Fus. Eng. Des. 54 (2001) 181–247.
[15] R. Bastasz, J.A. Whaley, Surface composition of liquid metals and alloys, Fus. Eng. and Des. 72 (2004) 111–119.
[16] J.P. Allain, D.N. Ruzic, M.R. Hendricks, D, He and Li sputtering of liquid eutectic Sn-Li, J. Nucl. Mater. 290–293 (2001) 33–37.

[17] F. Tabares, E. Oyarzabal, A.B. Martin-Rojo, et al., Experimental tests of LiSn alloys as potential liquid metal for the divertor target in a fusion reactor, Nucl. Mater. Energy 12 (2017) 1368–1373.
[18] M. Suchonova, J. Kristof, M. Pribula, et al., Analysis of LiSn alloys at different depths using LIBS, Fus. Eng. Des. 117 (2017) 175–179.
[19] S. Sharafat, N. Ghoniem, Summary of Thermo-Physical Properties of Sn and Compounds of Sn–H, Sn–O, Sn–C, Sn– Li, Sn–Si and Comparison of Properties of Sn, Sn–Li, Li, Pb–Li, Technical Report UCLA-UCMEP-00-31, University of California, 2000.
[20] F. Tabares, E. Oyarzabal, D. Tafalla, et al., Comparative studies of liquid metals for an alternative divertor target in a fusion reactor, Phys. Scr. T170 (2017), 014054.
[21] J. Loureiro, M. Fernandes, F.L. Tabares, et al., Deuterium retention in tin and lithium-tin samples exposed to ISTTOK plasmas, Nucl. Mater. Energy 12 (2017) 709–713.
[22] J. Ren, J.S. Hu, G.Z. Zuo, et al., A flowing liquid lithium limiter for the Experimental Advanced Superconducting Tokamak, Rev. Sci. Instrum. 86 (2015), 023504.
[23] D.N. Ruzic, W. Xu, D. Andruczyk, et al., Lithium–metal infused trenches (LiMIT) for heat removal in fusion devices, Nucl. Fusion 51 (2011), 102002.
[24] G.Z. Zuo, J. Ren, J.S. Hu, et al., Liquid lithium surface control and its effect on plasma performance in the HT-7 Tokamak, Fus. Eng. Des. 89 (2014) 2845–2852.
[25] P. Fiflis, A. Press, W. Xu, et al., Wetting properties of liquid lithium on select fusion relevant surfaces, Fus. Eng. Des. 89 (2014) 2827–2832.
[26] S. Krat, A. Popkov, Yu.M. Gasparyan, et al., Wetting properties of liquid lithium on lithium compounds, Fus. Eng. Des. 117 (2017) 199–203.
[27] E. Oyarzabal and F. L. Tabares, private communication.
[28] C.S. Baxter, Wettability of porous surfaces, Trans. Faraday Soc. 40 (1944).
[29] S. Hammouti, B. Holybee, M. Christenson, et al., Wetting of liquid lithium on fusion-relevant materials microtextured by femtosecond laser exposure, J. Nucl. Mater. 508 (2018) 237–248.
[30] A. Vertkov, I. Lyublisnki, M. Zharkov, et al., Liquid tin limiter for FTU tokamak, Fus. Eng. Des. 117 (2017) 130–134.
[31] P.F. Tortorelli, O.K. Chopra, Corrosion and compatibility considerations of liquid metals for fusion reactor applications, J. Nucl. Mater. 103–104 (1981) 621–632.
[32] R.N. Lyon, Liquid Metals Handbook, 2nd ed., Atomic Energy Commission, Department of the Navy, Washington, D. C., 1952.
[33] X. Meng, G. Zuo, W. Xu, et al., Effect of temperature on the corrosion behaviors of 304 stainless steel in static liquid lithium, Fus Eng. Des. 128 (2018) 75–81.
[34] M. Kondo, M. Ishii, T. Muroga, Corrosion of steels in molten tin, gallium and tin-lithium alloy, Fus. Eng. Des. 98–99 (2015) 2003–2008.
[35] K. Natesan, W.E. Ruther, Fabrication and properties of a tin–lithium alloy, J. Nucl. Mater. 307–311 (2002) 743–748.
[36] R.G. Wilson, SIMS quantification in Si, GaAs and diamond, an update, Int. J. Mass Spectrom. Ion Processes 143 (1995) 43–49.
[37] P.F. Tortorelli, J.H. De Van, Thermal-gradient mass transfer in lithium-stainless steel systems, J. Nucl. Mater. 85–86 (1979) 289–293.
[38] T. Emmerich, C. Schroer, Corrosion in austenitic steels and nickel-based alloys caused by liquid tin at high temperature, Corros. Sci. 120 (2017) 171–183.
[39] T.E. Everhart, P.H. Hoff, Determination of Kilovolt electron energy dissipation vs penetration distance in solid materials, J. Appl. Phys. 42 (1971) 5837.
[40] M. Szott, M. Christenson, H. Sandefur et al., Advancement in LiMIT and associated technologies, Oral presentation in 27th Symposium on Fusion Engineering, SOFE-27, Shanghai, China, 2017.
[41] A. de Castro, C. Moynihan, S. Stemmley, et al., Tin-lithium alloy/tin wetting investigations on 316 stainless steel, molybdenum, and tungsten. Oral presentation in 6th International Symposium on liquid metal applications for Fusion, ISLA-6, University of Illinois at Urbana Champaign, USA, 2019.
[42] M. Szott, Advanced Geometries for Dryout Mitigation in TEMHD-driven Liquid Lithium SYSTEMS, PhD Thesis, University of Illinois at Urbana-Champaign, 2020.
[43] C.A. Hart, C.H. Skinner, A.M. Capece, et al., Sorption of atmospheric gases by bulk lithium metal, J. Nucl. Mater. 468 (2015) 71–77.
[44] B.G. del Rio, G.S. Gautam, E.A. Carter, Deuterium addition to liquid Li-Sn alloys: implications for plasma-facing applications, Nucl. Fusion 60 (2020), 016025.
[45] W. Ou, R.S. Al, J.V.M. Vernimmen, et al., Deuterium retention in Sn-filled samples exposed to fusion-relevant flux plasmas, Nucl. Fusion 60 (2020), 026008.
[46] S. Brezinsek, J.W. Coenen, T. Schwarz-Selinger, et al., Plasma-wall interaction studies within the EURO-fusion Consortium: progress on plasma facing components development and qualification, Nucl. Fusion 57 (2017), 116041.
[47] P. Fiflis, L. Kirsch, D. Andruczyk, et al., Seebeck coefficient measurements on Li, Sn, Ta, Mo and W, J. Nucl. Mater. 438 (2013) 224–227.
[48] P. Rindt, J. Mata Gonzalez, P. Hoogerhuis, et al., Using 3D printing to optimize liquid metal divertor targets for flow and thermal stresses, Nucl. Fusion 59 (2019), 054001.